DR RICHARD M LAINE (Orcid ID : 0000-0003-4939-3514)

Article type : Article

t-ZrO_2 toughened Al_2O_3 free-standing films and as oxidation mitigating thin films on silicon nitride via colloidal processing of flame made nanopowders (NPs)

*Xinyu Zhang,[1] Xiaopo Cheng,[1] Monika Jansohn,[1] Matthias Niedermaier,[1,2] Thomas Lenk,[1,3] Stefan Britting,[4] Karsten Schmidt[4] and Richard M. Laine[1,]**

[1]Materials Science and Engineering, University of Michigan, Ann Arbor, MI 48109-2136, USA.

[2]Chemistry and Physics of Materials, Paris-Lodron University of Salzburg, Salzburg, A-5020, Austria.

[3]Professorship of Chemical Technology, Chemnitz University of Technology, 09111 Chemnitz, Germany.

[4]Rogers Germany GmbH, 92676 Eschenbach in der Oberpfalz, Germany.

*E-mail: talsdad@umich.edu

Keywords: ZTA, LF-FSP, nanopowders, tetragonal zirconia, power electronic substrates, Si_3N_4

Abstract

Zirconia toughened aluminas (ZTAs) are one of the most important engineering ceramics with high melting points, excellent mechanical strength and chemical stability, and are commonly used as wear resistant and high-temperature components, as prosthetic implants and electric circuit substrates. In this work, we explore methods of processing fine-grained, dense, thin, free-standing $(ZrO_2)_x(Al_2O_3)_{1-x}$ films (x = 0-50 mol. %, ~40 μm thick) by sintering flame made nanopowders (NPs) to optimize the *t*-ZrO_2 content, sinterability and microstructures under select conditions

(1120-1500 °C/5 h in O_2 or 95 %N_2/5 %H_2). In all cases, the final sintered products retain *t*-ZrO_2 with average grain sizes (AGSs) of 0.1-1 μm. ZTA film thicknesses were increased to ~200 μm to assess potential as electronic substrates. Excellent fracture toughness (24 MPa $m^{1/2}$) and small AGSs of 0.7 μm were found for ~200 μm thick ZTA films sintered at 1500 °C/5 h/N_2/H_2 using a three-step binder burnout process. Furthermore, we show that homogeneous ZTA thin films (<5 μm thick) can be sintered on Si_3N_4 substrates (thickness ≈ 300 μm) to provide physical protection against oxidation under extreme conditions (1500 °C/1 h/O_2), offering additional practical utility for high-temperature ceramics and power electronic substrates.

Introduction

Alumina (Al_2O_3) is a widely studied structural ceramic with applications as grinding media, for cutting tools, high-temperature engine components, prosthetic implants, and substrates for power electronics due to its high melting point, excellent mechanical strength, hardness and chemical stability as well as its widespread abundance.[1–17] However, applications using pure α-Al_2O_3 are limited by its low resistance to crack propagation, i.e., poor fracture toughness (4-5 MPa $m^{1/2}$)[18,19] that can lead to catastrophic failure.[1–3] To enhance Al_2O_3 fracture toughness, a common practice involves incorporating additives such as tetragonal zirconia (*t*-ZrO_2) to increase toughness while maintaining the hardness and chemical resistance of Al_2O_3, commonly referred to as zirconia toughened aluminas (ZTAs).[2–6,20–29]

Room temperature stabilized *t*-ZrO_2 will transform to monoclinic (*m*-ZrO_2) if subjected to mechanical stress. This transformation is accompanied by a 4 % volume expansion creating a compressive stress field in the surrounding grains, which opposes crack propagation.[2–4,20–24] In this process some fraction of the energy needed for crack propagation is consumed promoting the $t \rightarrow m$, transformation, the operative mechanism that inhibits crack propagation.[21–24] Unfortunately, *t*-ZrO_2 typically transforms to *m*-ZrO_2 at 950-1000 °C on cooling making it unstable at lower temperatures.[2–4,20–24] A resolution to this problem is to stabilize *t*-ZrO_2 by introducing dopants with cationic radii close to that of Zr^{4+} (0.8-1 Å, e.g. Y^{3+}, Ca^{2+}, Mg^{2+} and related rare earth ions).[2,6–8,21–23,26,30–33] Table **1** compares various ZTA compositions synthesized/sintered using different methods and their selected properties. In general, yttria (Y^{3+}) is the most common dopant, stabilizing *t*-ZrO_2 after sintering at 1600 °C/1-5 h/air (Table **1**).[2,6,21]

Previously, we demonstrated that it is possible to sinter flame made nanopowders (NPs, average particle sizes, APSs: 40-60 nm) consisting of particles of t-ZrO_2 encapsulated within δ-Al_2O_3 shells to fully dense $(t\text{-}ZrO_2)_{0.54}(\alpha\text{-}Al_2O_3)_{0.46}$ pellets (diameter = 13 mm, thickness = 1.4 mm) with AGSs ≤200 nm at 1120 °C/6 h/air. The encapsulation process seems to stabilize the t-ZrO_2 without the need for additives likely due to rapid quenching of the flame made NPs (liquid feed flame spray pyrolysis, LF-FSP) to kinetically rather than thermodynamically stable phases produced using traditional processing methods.[27–29]

We have recently returned to these flame made NPs, demonstrating their utility as a simple and scalable route to functional ceramic thin films (<100 μm thick) for applications such as capacitors, solid electrolytes and electrodes for solid-state batteries.[34–36] Coincidentally, we reported processing dense and flexible α-Al_2O_3 thin films (<10 μm).[10]

Our success with α-Al_2O_3 thin films prompted efforts to extend our new approach to t-ZrO_2 doped α-Al_2O_3 thin films targeting mechanical properties superior to α-Al_2O_3 for applications including electronic substrates and protective coatings.

In the first part of the present work, we explored sintering $(ZrO_2)_x(Al_2O_3)_{1-x}$ thin films (x = 0-50 mol. %, ~40 μm thick) using a select set of conditions (1120-1500 °C/5 h in O_2 or 95 %N_2/5 %H_2) from NPs by LF-FSP to optimize ZrO_2 content, sinterability and microstructures. Similar to our previous work,[27–29] all films retain t-ZrO_2 at RT with AGSs of 0.1-1 μm.

Although no t-ZrO_2 stabilizing additives are needed due to rapid quenching of LF-FSP, additives such as TiO_2 and MgO were found to be effective in tailoring final grain sizes and sinterability; permitting us to optimize the ZTA composite properties. Studies show that TiO_2 doping enhances densification and reduces ZTA sintering temperatures on substituting Al^{3+} by Ti^{4+} which generates vacancies, thereby improving diffusion.[7,37–40] Additionally, Chen *et al.*[7,8] report formation of a liquid phase at ZTA grain boundaries with TiO_2 contents ≥4 wt. % which also promotes densification. Unfortunately, TiO_2 doping sometimes coincides with excessive grain growth leading to a reduced elastic modulus and hardness.[7,8,37] Consequently, we sought to eliminate this issue by introducing MgO, which is quite useful in limiting grain sizes in the α-Al_2O_3 thin films.

MgO is known to be an effective additive in inhibiting grain growth during sintering through segregation of MgO-Al_2O_3 solid solutions (solubility limit ≈ 500 ppm MgO) and/or pinning through formation of fine spinel particles ($MgAl_2O_4$) at grain boundaries resulting in reduced grain

boundary mobility.[10,40–51] It has also been suggested that the dominant densification mechanism is via surface diffusion for MgO doping levels of 0.1-0.3 wt. %, and grain boundary diffusion for MgO concentrations of 0.5-1.0 wt. %.[47,48] In this work, both TiO_2 and MgO additives (~1 wt. % each) were used to optimize sinterability and final microstructures.

While thin films are suitable for applications such as electronic devices and protective coatings, for other structural applications such as wear components, dental composites and prosthetic implants, bulk materials are also highly desirable. At the interface between bulk and thin films, intermediate thicknesses, e.g. up to ~300 μm are used as electrically insulating layers as well as high-strength substrates for piezoresistive sensors and power electronics.[11–14] Finally, to test ZTA mechanical properties, greater thicknesses are preferred to prevent cracking caused simply by handling.

These issues provided the motivation to expand our approach to ZTA films up to ~200 μm thick and up to ~ 2×2 cm^2. To our surprise, ~200 μm thick ZTA films doped with MgO and TiO_2 (1 wt. % each) show a fracture toughness of 24 MPa $m^{1/2}$ using single-edged precracked beam tests (SEPB), which is 2-4 times higher than reported values (Table **1**), suggesting potential application as electronic substrates with improved mechanical properties.

Similar to ZTA films, silicon nitride (Si_3N_4) films (~300 μm thick) are also commonly used in structural applications due to their good chemical, physical and thermal stabilities, and mechanical properties.[15,16,52–58] For electronic substrates, Si_3N_4 films exhibit superior thermal conductivity (κ) of ~90 W/mK (at RT) and a K_{1C} of 6.5-7 MPa $m^{1/2}$ compared to ZTA films (typically κ = 28 W/mK and $K_{1C} \approx 5$ MPa $m^{1/2}$) providing better thermal conductivity and reliability.[15,57]

Unfortunately, Si_3N_4 is susceptible to oxidation even at ambient and may deteriorate over time.[52–55] Although a surface oxide/oxynitride layer that forms can protect against further oxidation,[52,53] to withstand high-temperature oxidation and/or active oxidation environments, additional protection is needed. In the present work, we find that sintered ZTA coatings (<5 μm) adhere well to Si_3N_4 substrates (thickness ≈ 300 μm) providing physical protection against oxidation after heating to 1500 °C/1 h/O_2 as characterized by scanning electron microscope (SEM).

Experimental procedures

Precursor syntheses

Nanopowders (NPs) were produced by liquid feed-flame spray pyrolysis (LF-FSP), which was invented in the Laine group at the University of Michigan. It is a single-step continuous synthesis method for producing ceramic NPs. Typical metalloorganic precursors in this work include metal-carboxylates and metal-atrane compounds; detailed synthesis procedures are reported elsewhere.[10,27–29,34–36,59–62] Representative examples are provided in the Supporting Information (SI).

Liquid-Feed Flame Spray Pyrolysis (LF-FSP)

Metalloorganic precursors at selected compositions were dissolved in alcohol, usually ethanol, at 1-10 wt. % solids loading. The solution is fed (30-80 ml min^{-1}) into an atomizing nozzle (BETE XA-PR, Greenfield, MA) and aerosolized with oxygen (80 psi, 40 ml min^{-1}) into a quartz chamber where it is ignited with methane/oxygen (40 ml min^{-1}/30 ml min^{-1}) pilot torches on the spray head. Oxygen shield gas (150 ml min^{-1}) provides an oxygen-rich environment to minimize carbon residues. Initial combustion takes place producing temperatures of ≥1500 °C followed by a quenching step that drops the temperature to 300-500 °C over 1.5 m, equivalent to a 1000 °C quench in <100 ms, to produce NPs. Powders are collected downstream in rod-in-tube electrostatic precipitators (ESP) operating at 10 kV. Scheme **1** illustrates the LF-FSP apparatus for NP production.

As-produced NPs were then dispersed in ethanol (200 proof, Decon Labs, King of Prussia, PA) using an ultrasonic horn (Vibra cell VC-505, Sonics & Materials Inc. Newtown, CT) at 100 W/10 min. The suspension was allowed to settle for 5 h to remove larger particles. The supernatant was decanted and allowed to oven dry (60 °C/12 h) providing the starting ZrO_2 doped δ-Al_2O_3 NPs.

Film processing

Generally, LF-FSP synthesized NPs were mixed with polymeric additives such as binder, plasticizer, curing agent, and dispersant, in a selected solvent system by ball-milling (Rotary Tumbler Model B, Tru-Square Metal Products) using 3.0 mm diameter spherical Al_2O_3 as the milling media. One fifth of the container (20 ml) was filled with the milling media (~6 g). An example suspension of ZrO_2 doped Al_2O_3 is given in Table **S1**.

The suspensions were cast on Mylar film using a wire-wound rod coater (Automatic Film Applicator-1137, Sheen Instrument, Ltd. Santa Fe Springs, CA). The cast thickness was adjusted to 100-255 μm to control the thickness of the final ceramic film. A glass cover was used to control the solvent drying rate to avoid mud cracking.

After solvents evaporated, dried green films were uniaxially pressed between stainless steel dies at 100 °C at 10 ksi/5-30 min using a heated benchtop laboratory manual press (Model 3851-0, Carver, Inc., Wabash, IN) to improve packing density.[10,34–36] One/two layers for thin films (thickness ≈ 20-80 μm) and 8-10 layers for thick films (thickness ≈ 200 μm) were pressed together.

Film sintering

Green films (typically 5 × 5 mm^2) were placed between two Al_2O_3 substrates (diameter = 42 mm) and sintered to selected temperatures, times and ramp rates, using a vacuum tube furnace (GSL-1600X, Richmond, CA). The substrates were used to prevent warping of the ceramic films.

Films were subject to binder burnout process prior to sintering by heating them to 800 °C/1 h in extra dry grade O_2 (60 ml min^{-1}). Subsequently, they were sintered at various conditions: 1120-1500 °C at 1-10 °C min^{-1} under a constant gas (O_2 or 95%N_2/5%H_2) flow of 60 ml min^{-1}. For convenience, 95%N_2/5%H_2 is referred to as N_2/H_2 in the following sections. Typical sintering schedules are given in Figure **S1**.

Coating Si_3N_4 substrates

Suspensions of 10 mol. % ZrO_2 doped δ-Al_2O_3 for coating Si_3N_4 substrates (Rogers Corp.) were prepared per Table **S2**.

Si_3N_4 films were coated one side at a time. The suspension was first cast on one side of Si_3N_4 samples with 25 μm spacers using the coating setup shown in Figure **S2**; then the films were thermally pressed at 100 °C bottom, 60 °C top, 8 ksi. They were sintered in two steps: binder burnout at 800 °C/1 h/O_2; and sintering at 1500 °C/5 h/N_2/H_2 (Figure **S1b**) The other side of the films was then coated and sintered following the same procedure.

Results and discussions

In the following sections, we first characterize microstructures, sinterability and phase compositions of ZTA thin films (~40 μm) derived from $(ZrO_2)_x(Al_2O_3)_{1-x}$ (x = 0-50 mol. %) NPs sintered under select conditions. Film thicknesses were then increased to ~ 200 μm to explore their potential utility as substrates for power electronics. The effects of different sintering conditions were explored to minimize cracking while optimizing microstructures and densities. Finally, ZTA coatings on Si_3N_4 substrates were processed and optimized as characterized by a dye penetration test, an oxygen damage test, XRD and SEM.

ZTA ~40 μm thin films

To identify the mix of phases required to optimize the properties of the final sintered products, $(ZrO_2)_x(Al_2O_3)_{1-x}$ (x = 0, 15, 30, 50 mol. %) NPs were produced by LF-FSP. APSs and specific surface areas (SSAs) were calculated using BET data (see experimental) per Table **2**. All NPs show similar SSAs of 40-50 m^2/g and APSs of ~30 nm; $(ZrO_2)_{0.3}(Al_2O_3)_{0.7}$ shows the lowest APS of 25 nm. Figure **S3** shows SEMs of as-produced Al_2O_3 and $(ZrO_2)_{0.5}(Al_2O_3)_{0.5}$ NPs, both exhibit a broad size distribution with APSs <50 nm, and a few particles >100 nm that are likely agglomerated in overall agreement with Table **2** APSs. Nanosized powders with log normal particle size distributions are advantageous for processing in that they reduce sintering temperatures due to high surface energies and provide high packing densities.

Figure **1** compares XRDs of as-produced $(ZrO_2)_x(Al_2O_3)_{1-x}$ NPs. As produced LF-FSP Al_2O_3 is a mixture of δ-Al_2O_3 phases, as expected from previous work.[10,27,59] For ZrO_2 (x > 0 mol. %) doped Al_2O_3, a mixture of δ-Al_2O_3 and *t*-ZrO_2 is observed, as previously reported for $(t\text{-}ZrO_2)_x(\delta\text{-}Al_2O_3)_{1-x}$ (x = 0.02-0.8) core-shell NPs.[27–29]

Figure **2** compares SEMs of $(ZrO_2)_x(Al_2O_3)_{1-x}$ thin films (40-60 μm thick) sintered under different conditions in O_2 (see Figure **S1a** schedule). All films show uniform grain sizes (100-500 nm, Figure **3**), AGSs and densities increase with the sintering temperature, but pores are not fully eliminated even at 1500 °C.

Figure **3a** suggests that grain sizes decrease slightly with increasing ZrO_2 content, although the difference for higher contents is not significant. As seen in Figure **3b**, film thicknesses decrease with increasing sintering temperature. Overall, the 30 mol. % ZrO_2 film shows the smallest final AGSs and the greatest decrease in thickness at higher temperatures.

Previous reports indicate that sintering α-Al_2O_3 in a hydrogen atmosphere improves densification and reduces porosity.[10,63] These results prompted efforts here to sinter thin $(ZrO_2)_x(Al_2O_3)_{1-x}$ (x = 15, 30, 50 mol. %) films in N_2/H_2 following a two-step procedure per Figure **S1b**: binder burnout at 800 °C/1 h/O_2 and sintering at 1400 °C/5 h/N_2/H_2. As shown in Figure **S4**, compared to films sintered in O_2 (Figure **2**), an N_2/H_2 atmosphere improves densification slightly, and AGSs appear to be smaller. However, the films are porous suggesting incomplete densification.

As demonstrated in Figures **2** and **3**, 30 mol. % ZrO_2 doped Al_2O_3 films show limited grain growth and the most significant decrease in thickness on sintering at 1400-1500 °C compared to other compositions. As discussed in the introduction, TiO_2 doping improves Al_2O_3 densification but increases grain sizes,[7,8,37–40] while MgO limits grain growth.[10,40–51] Therefore, to further

improve sinterability, the effects of TiO_2 and MgO additives (1 wt. % each) to 30 mol. % ZrO_2 doped Al_2O_3 were investigated.

As seen in Table **3**, we studied sintering effects of two different TiO_2 powders (1 wt. % doping): TiO_2 commercial powder (CP, claimed APS ≈ 20 nm), and TiO_2 NP by LF-FSP (APS = 20-30 nm). For composition **D**, MgO doping was introduced by mixing LF-FSP produced 30 mol. % ZrO_2 doped Al_2O_3 and 2 wt. % MgO doped Al_2O_3 NPs, the resulting mixture has a 10 mol. % ZrO_2 and ~1 wt. % MgO content. MgO (2 wt. %) doped Al_2O_3 NP was chosen based on work by Takeuchi *et al*.[10] that generated dense and flexible sintered thin films (<10 μm). The ZrO_2 content was reduced because typical power electronic ZTA substrates contain <30 mol. % ZrO_2.[13–15]

Figure **4** compares the SEM fracture surfaces of films **A**-**D** (Table **3**) sintered at 1300-1500 °C/5 h/O_2 (Figure **S1a**). At 1300 °C, all films are not dense, but the grains of 30 mol. % ZrO_2 doped Al_2O_3 supplemented with TiO_2 (**B** and **C**) show significant grain growth compared to films without TiO_2 (**A**) as expected.[7,8,37–40] In contrast, the Al_2O_3 film doped with 10 mol. % ZrO_2, 1 wt. % TiO_2 NP and MgO (**D**) shows small AGSs which are comparable to film **A**, a result of MgO doping that prevents excessive grain growth.[10,40–51]

At 1400 °C, films 30 mol. % ZrO_2 doped Al_2O_3 supplemented with TiO_2 (**B** and **C**) are already dense with intergranular fracture surfaces. The Al_2O_3 film with 10 mol. % ZrO_2 (**D**) starts to densify. At 1450 °C, films **B** and **C** show abnormal grain growth; the 30 mol. % doped Al_2O_3 without TiO_2 (**A**) starts to densify with uniform grain sizes.

These films show significant differences in AGSs when sintered at 1500 °C per Figure **4** bottom. Film **A** shows a rather small AGSs of ≈ 200 nm with visible pores. Excess grain growth is exhibited in film **B** (AGSs ≈ 1-2 μm). Films **C** and **D** show similar AGSs of ~500 nm. Film **D** exhibits some transgranular (intra-) fracture behavior (marked with red arrow) suggesting improved mechanical properties at grain boundaries.

Figure **5** presents the XRDs of the films sintered at 1300-1500 °C/5 h/O_2. The films consist mainly of α-Al_2O_3 (corundum, hexagonal, space group 167, PDF-98-001-1217) and *t*-ZrO_2 (tetragonal, space group 137, PDF-04-013-6616); some films show small peaks at 36, 40, 48 and 49° 2θ (not marked in Figure **5**) corresponding to a calcite phase (hexagonal, space group 167), which is likely a result of residual carbon from insufficient O_2 during LF-FSP. Overall, no *m*-ZrO_2 is observed; similar phases are exhibited for films with different compositions and sintering conditions.

A similar sintering study on the films **A**-**D** was repeated in N_2/H_2 (see Figure **S1b** schedule). Since the films barely sinter at 1300 °C/5 h/O_2 (Figure **4**), a similar outcome in N_2/H_2 is expected and therefore only sintering at 1400-1500 °C/5 h/N_2/H_2 was explored.

Figure **6** compares SEM fracture surfaces of films **A**-**D** sintered at 1400-1500 °C/5 h/N_2/H_2. Similar densification behaviors are observed as in O_2. Films **B** and **C** start to densify at 1400 °C, obvious grain growth can be seen at 1500 °C, especially for film **B**. Films **A** and **D** show similar sintering behavior, they densify at 1500 °C, and exhibit finer grain sizes (~0.5-1 μm) than **B** and **C** (≥ 1 μm). As discussed, TiO_2 promotes grain growth and densification,[7,8,37–40] while MgO tends to diffuse to the grain boundaries and limits grain growth.[10,40–51]

After sintering at 1500 °C, all films show some transgranular fracture behavior (marked with red arrows) suggesting improved mechanical properties.

Film lateral shrinkage was measured before and after sintering per Table **4**. Overall, shrinkage increases with sintering temperature. At 1500 °C in both O_2 and N_2/H_2, films with different compositions show similar lateral shrinkages of ~20 %. Films with composition **B** have the highest lateral shrinkage, recall that they have much larger AGSs (1-2 μm at 1500 °C/O_2 and N_2/H_2), as seen in Figures **4** and **6**. This suggests, as expected, that TiO_2 CP promotes densification and grain growth, resulting in higher shrinkages and larger AGSs. TiO_2 LF-FSP NPs also promote densification (Figures **4** and **6**), film **C** starts to densify at 1400 °C, but smaller AGSs result compared to film **B**, likely a result of the smaller APSs of TiO_2 LF-FSP NPs compared to TiO_2 CP. Film **D** with both TiO_2 and MgO doping generally shows both smaller and more uniform AGSs compared to film **C** under different sintering conditions (Figures **4** and **6**).

Figure **S5** shows XRDs of the films sintered at 1400-1500 °C/5 h/N_2/H_2. Similar to films sintered in O_2, they mainly contain α-Al_2O_3 and *t*-ZrO_2; the impurity calcite phase (36, 40, 48 and 49° 2θ) is also observed in some films. Phase compositions of the different films are also very similar, and no *m*-ZrO_2 is observed. The composition does not change with different sintering conditions.

The conclusions from the thin film work are that films with composition **D** per Table **3** show small and uniform grain sizes (0.5-1 μm), and low porosity. They are almost fully dense when sintered at 1500 °C/5 h, in either O_2 or N_2/H_2 per SEM observations (Figures **4** and **6**). These results were then extended to processing ~200 μm thick ZTA films with the same composition.

ZTA ~200 μm thick films

In this section, the sinterability, microstructures and fractural toughness of ZTA films up to ~200 μm thick and ~2×2 cm^2 were investigated for possible application as power electronic substrates[11–14] using composition **D** from the above studies.

We first started by targeting ~200 μm thick ZTA films with small sizes (~1×1 cm^2) sintered at 1500 °C/5 h in O_2 or N_2/H_2 to compare sintering behavior in different atmospheres. Figure **7** compares SEM fracture surfaces of ZTA films (composition **D**) sintered at 1500 °C/5 h in O_2 and N_2/H_2. Films sintered in different atmospheres show similar morphologies with AGSs of 0.5-1 μm. Films sintered in N_2/H_2 shows slightly smaller AGSs, greater shrinkage in both lateral and vertical dimensions (Figure **7** and Table **5**), and lower porosity (Figure **7d** *vs*. **7c**), suggesting that N_2/H_2 provides higher densities, in agreement with previous work on MgO (0-5 wt. %) doped Al_2O_3 thin films.[10]

Figure **S6** shows XRDs of ZTA films (composition **D**) sintered in O_2 and N_2/H_2, respectively. Similar to thin films above, both films exhibit two main phases: α-Al_2O_3 (hexagonal) and *t*-ZrO_2, but the impurity phase (calcite) disappears. No obvious difference in phase compositions is observed for films sintered in different atmospheres.

Studies on smaller (~1×1 cm^2), ~200 μm ZTA films suggested that N_2/H_2 sintering provides higher densities. Therefore, we continued studies on larger films (~2×2 cm^2) sintered in N_2/H_2. Initially, the same sintering schedule with a ramp rate of 5 °C/min was used (Figure **S1b**). However, as seen in Figure **S7**, the larger films cracked while smaller films remained intact after sintering.

It's likely that the fast ramp rate leads to fast shrinkage and cracking. Therefore, the ramp rate was reduced to 2.5 and then 1 °C/min while following the same schedule per Figure **S1b**, but the larger films still cracked (Figure **S7**). Only one large film out of three sintered at 1 °C/min was crack-free. This suggests that a slow ramp rate will prevent cracking, but it is a very inefficient method (long sintering time: >24 h) that provides small improvements.

In addition, these films bonded to the Al_2O_3 substrates after sintering, a likely source of stress that results in cracking. Therefore, an insulating boron nitride (BN) powder layer was introduced as it is stable to ~2000 °C, see below.

SEMs of ~200 μm ZTA films sintered at different ramp rates show small differences (Figure **8**). All films were dense with similar AGSs of 1-2 μm. However, films sintered at lower ramp rates (2.5 and 1 °C/min) show slightly larger grains (Figure **8** and Table **6**), likely due to the longer

sintering times. The sintered thicknesses varied between 175-210 μm. Table **6** summarizes AGSs, shrinkage and density changes on sintering.

Generally, slower ramp rates caused greater shrinkages and higher densities, but overall densities (~90 %) are low while AGSs increased compared to small films per Figure **7** and Table **5**, likely due to undesired adherence of the ZTA films to the Al_2O_3 substrates inhibiting shrinkage and therefore densification, while coincidentally generating larger AGSs.

Figure **S8** compares XRDs of ~200 μm ZTA films sintered at different ramp rates. No obvious differences can be seen; all the films show two main phases without impurities: α-Al_2O_3 and *t*-ZrO_2.

To eliminate cracking, an insulating BN layer (powder from Sigma-Aldrich) was introduced to prevent bonding with the Al_2O_3 substrates. Additionally, sintering following different binder burnout temperatures of 600°, 800° and 1100 °C was investigated. The binder burnout atmosphere was changed from O_2 to air reducing the rate of oxidative decomposition. The sintering schedule is provided in Figure **S9**.

Figure **S10** compares films sintered at different binder burnout temperatures with BN interfaces. Films debindered at 800 °C/1 h/air stayed mostly intact after sintering. However, films debindered at 600 °C/1 h/air formed large cracks, and films debindered at 1100 °C/1 h/air cracked into pieces. Such differences in film quality suggest that cracking is primarily related to binder burnout.

Figure **S11** compares SEMs of ~200 μm ZTA films with different binder burnout temperatures with BN insulation. Films debindered at 600 °C/1 h/air show the lowest porosities and smallest AGSs of 0.7 μm among the three (Table **7**). All films show similar vertical shrinkages of ~20 % (Table **7**). Figure **S12** compares XRDs of 200 μm ZTA films with different binder burnout temperatures. As with the above XRD studies, no obvious differences are observed; all films show two main phases of α-Al_2O_3 and *t*-ZrO_2 without impurity.

To further investigate the binder burnout mechanism, a TGA-DTA was run on the 10 mol. % ZrO_2 doped Al_2O_3 green films (composition **D**, Figure **S13**). A decomposition exotherm for the organics appears between ~180-500 °C. Accordingly, the sintering schedule was modified per Figure **S14** with a three-step binder burnout procedure: first holding at 200 °C/1 h and slowly (1 ° C/min) ramping up to 500 °C, then ramping up (2.5 °C/min) to 800 °C/1 h.

Figure **9** shows optical images of ~200 μm ZTA films before and after sintering. After binder burnout, all films only show minimal size changes. Shrinkage and coincident densification occur

primarily during sintering. Films with thicknesses ≤200 μm after sintering are crack-free, while films with thicknesses >220 μm exhibit small cracks. All films remain mostly intact with better quality compared to the above films (Figures **S7** and **S10**).

As shown in Figure **10**, films sintered using the 3-step binder burnout procedure show low porosities and small AGSs of 0.7 μm after sintering. Table **7** compares AGSs, shrinkages and densities of ZTA films sintered using different binder burnout conditions with BN insulation. All films have densities of 97-99 % determined by Archimedes method, which improve significantly from films sintered without BN insulation (~90 % dense, Table **6**). In addition, the AGSs of films sintered with BN decreased (≤1 μm) compared to films without (1.3-1.6 μm, Table **6**). The use of BN powder between ZTA films and Al_2O_3 improves film densities and reduces AGSs, as the substrate effects are eliminated.

Fracture toughness (K_{1C}) measurements were undertaken using a single-edge precracked beam test (SEPB) on the ~200 μm ZTA films (composition **D**) sintered with a 3-step binder burnout procedure (Figure **S14**) as they show optimum qualities compared to other films. As given in Figure **S15**, ~200 μm 10 mol. % ZrO_2 doped Al_2O_3 films show K_{1C} values in a range of 15-38 MPa $m^{1/2}$ (three samples) with an average of 24 MPa $m^{1/2}$, which is 2-4 times higher than reported values. Such a high K_{1C} value may be attributed to the fine and uniform ceramic microstructures sintered from NPs by LF-FSP, retained *t*-ZrO_2 phase after sintering, TiO_2 and MgO doping, and improved film qualities through sintering refinement.

Coating Si_3N_4 substrates with ZTA thin films

In this section, above results provide the basis for formulating and processing thin ZTA films (composition **D** per Table **3**) on ~300 μm Si_3N_4 films as a bonded physical layer to minimize oxidation for high-temperature substrates and power electronic applications. As discussed in the previous section, ZTA films with composition **D** show a high K_{1C} and density, therefore we continued coating studies with the same composition.

Figure **11a** shows surfaces of coated Si_3N_4 films sintered at 1500 °C/5 h/N_2/H_2. Compared to uncoated films in Figure **S2**, the coating appears to be light grey and uniform. As shown in Figure **11b**, a coated Si_3N_4 film was marked with red dye and then rinsed with ethanol. After rinsing, the red mark disappears completely, which suggests that the die does not penetrate through unseen cracks and that the coating is stable, smooth and crack free.

Figures **12** and **S16** show SEMs and EDSs of coated Si_3N_4 films. For coated films, the rod-like Si_3N_4 structure at the surface (Figure **12c**) is replaced by a dense, homogeneous Al-rich coating with finer grains (Figures **12b** and **S16**). The fracture surface suggests the coating is 2-3 μm thick (Figure **12a**). However, there are small cracks propagating along the surface (Figure **12b**), which may be introduced by thermal pressing or the sample breaking during SEM preparation, which requires small sample sizes (≤0.5×0.5 cm^2).

As shown in the Figure **13** XRDs, coated Si_3N_4 films present hexagonal β-Si_3N_4, as found in the original Si_3N_4 film. A cubic γ-$Al_{2.66}O_4$ phase appears with a trace of cubic ZrO_2, indicating that the 10 mol. % ZrO_2 doped Al_2O_3 likely reacts or partially reacts with the Si_3N_4 substrate resulting in a structural distortion again suggesting good bonding.

Uncoated and coated Si_3N_4 films were heated to 1500 °C/1 h/O_2 to assess resistance to oxidation. As shown in Figure **14**, the uncoated Si_3N_4 film suffers more damage than the coated sample. The edges of both films show more visible damage than the centers. During heating, films were sandwiched between Al_2O_3 substrates; the edges were more exposed to O_2 than the center. SEM surface images of the uncoated Si_3N_4 film reveal large cavities from obvious oxidation, while the coated film exhibits a smoother microstructure (Figure **14c** and **d**). Overall, it is evident that the coating protects Si_3N_4 films against oxidization, even under extreme conditions.

Conclusions

In summary, we investigated the sinterability, microstructures and phase compositions of ZTA thin films (~40 μm) with varying compositions and sintering conditions starting from $(ZrO_2)_x(Al_2O_3)_{1-x}$ (x = 0-50 mol. %) NPs by LF-FSP. Studies suggest that 1 wt. % MgO and TiO_2 additives improve the sintering behavior, resulting in dense films (composition **D**: 10 mol. % ZrO_2 doped Al_2O_3 with 1 wt. % TiO_2 and MgO) with final AGSs of 0.5-1 μm at 1500 °C. Comparison of films sintered in O_2 and N_2/H_2 suggests that the N_2/H_2 atmosphere improves film quality coincident with higher shrinkages and densities, and smaller reductions in AGSs.

For potential applications as power electronic substrates, ZTA film thicknesses were increased to 150-250 μm. Sintered films exhibit hexagonal *α*-Al_2O_3 and *t*-ZrO_2 phases, which in principle provide good mechanical properties, and was proved by SEPB test that a high K_{1C} value of ~24 MPa $m^{1/2}$ is obtained. By investigating the effects of different sintering conditions, we were able

to sinter crack-free 150-250 μm thick 10 mol. % ZrO_2 doped Al_2O_3 films with AGSs of 0.7 μm by using BN insulation between films and Al_2O_3 substrates with a three-step binder burnout procedure.

Finally, ZTA thin films (composition **D**) form homogenous coatings on Si_3N_4 substrates with thicknesses <5 μm that offer protection under extreme oxidative conditions (1500 °C/1 h/O_2), suggesting an alternate application of ZTA films for high-temperature ceramics and power electronic substrates.

Acknowledgment

We are grateful for the support of this work by Rogers Corp., as well as their provided Si_3N_4 substrates and fracture toughness SEPB test on ZTA films. We also thank Makoto Takeuchi for his effort on MgO doped (0-5 wt. %) Al_2O_3 thin films (<10 μm)[10] that provided motivation and help on the present work.

References

1. Dorre E, Heinz Hubner. Alumina: processing, properties and applications. Berlin Heidelberg: Springer-Verlag; 1984.

2. Rao PK, Jana P, Ahmad MI, Roy PK. Synthesis and characterization of zirconia toughened alumina ceramics prepared by co-precipitation method. Ceram Int. 2019;45(13):16054–61.

3. Isfahani T, Javadpour J, Khavandi A. Formation mechanism and phase transformations in mechanochemically prepared Al2O3-40wt% ZrO2 nanocomposite powder. Compos Interfaces. 2019;26(10):887–904.

4. Sarkar D, Mohapatra D, Ray S, Bhattacharyya S, Adak S, Mitra N. Synthesis and characterization of sol-gel derived ZrO2 doped Al2O3 nanopowder. Ceram Int. 2007;33(7):1275–82.

5. Sarkar D, Adak S, Mitra NK. Preparation and characterization of an Al2O3-ZrO2 nanocomposite, part I: powder synthesis and transformation behavior during fracture. Compos Part Appl Sci Manuf. 2007;38(1):124–131.

6. Ganesh I, Olhero SM, Torres PMC, Alves FJ, Ferreira JMF. Hydrolysis-induced aqueous gelcasting for near-net shape forming of ZTA ceramic composites. J Eur Ceram Soc. 2009;29(8):1393–401.

7. Zu Y, Chen G, Fu X, Luo K, Wang C, Song S, et al. Effects of liquid phases on densification of TiO2-doped Al2O3-ZrO2 composite ceramics. Ceram Int. 2014;40(3):3989–93.

8. Chen G, Zu Y, Luo J, Fu X, Zhou W. Microstructure and superplastic behavior of TiO2-doped Al2O3-ZrO2 (3Y) composite ceramics. Mater Sci Eng A. 2012;554:6–11.

9. Yu W, Zheng Y, Yu Y, Su X. Microstructural evolution of supra-nanostructure Al2O3/ZrO2 eutectic powders by combustion synthesis-spray cooling. J Am Ceram Soc. 2019;102(12):7689–98.

10. Takeuchi M, Niedermaier M, Jansohn M, Umehara N, Laine RM. Processing thin (<10μm), dense, flexible α-Al2O3 films from nanopowders. J Ceram Soc Jpn. 2019;127(2):81–9.

11. Gundel P, Persons R, Bawohl M, Challingsworth M, Czwickla C, Garcia V, et al. Highly reliable and cost effective thick film substrates for power LEDs. In: 2016 IEEE Applied Power Electronics Conference and Exposition (APEC) [Internet]. Long Beach, CA: IEEE; 2016. p. 3069–74. Available from: https://doi.org/10.1109/APEC.2016.7468301.

12. Maeder T, Jacq C, Ryser P. Long-term mechanical reliability of ceramic thick-film circuits and mechanical sensors under static load. Sens Actuators Phys. 2012 (Oct);186:210–8.

13. Srikanth C, Madhu GM. Effect of ZTA concentration on structural, thermal, mechanical and dielectric behavior of novel ZTA–PVA nanocomposite films. SN Appl Sci. 2020 (Mar);2(3):422.

14. Mussavi Rizi SH, Ghatee M. A study of mechanical properties of alumina–zirconia composite films prepared by a combination of tape casting and solution impregnation method. J Aust Ceram Soc. 2020 (Mar);56(1):167–74.

15. Miric A, Dietrich P. Inorganic Substrates for Power Electronics Applications. Heraeus Dtschl. 2013;1–7.

16. Chen I-W, Xue LA. Development of superplastic structural ceramics. J Am Ceram Soc. 1990 (Sep);73(9):2585–609.

17. Wang X, Padture NP, Tanaka H. Contact-damage-resistant ceramic/single-wall carbon nanotubes and ceramic/graphite composites. Nat Mater. 2004 (Aug);3(8):539–44.

18. Chen P, Chen J, Guo B, Liu H. Measurement of the dynamic fracture toughness of alumina ceramic. In: Song B, Lamberson L, Casem D, Kimberley J, editors. Dynamic Behavior of Materials, Volume 1 [Internet]. Cham: Springer International Publishing; 2016. p. 33–8. (Conference Proceedings of the Society for Experimental Mechanics Series). Available from: https://link.springer.com/chapter/10.1007/978-3-319-22452-7_6.

19. Casellas D, Nagl MM, Llanes L, Anglada M. Fracture toughness of alumina and ZTA ceramics: microstructural coarsening effects. J Mater Process Technol. 2003 (Dec);143–144:148–52.

20. Green DJ. Critical microstructures for microcracking in Al2O3-ZrO2 composites. J Am Ceram Soc. 1982;65(12):610–614.

21. Tuan WH, Chen RZ, Wang TC, Cheng CH, Kuo PS. Mechanical properties of Al2O3/ZrO2 composites. J Eur Ceram Soc. 2002;22(16):2827–33.

22. Dresvyannikov AF, Petrova EV, Khairullina AI. Electrochemical synthesis and physicochemical properties of nanostructured Al2O3–ZrO2–MgO oxide systems. Prot Met Phys Chem Surf. 2020;56(1):89–93.

23. Abi CB, Emrullahoğlu OF, Said G. Microstructure and mechanical properties of MgO-stabilized ZrO2-Al2O3 dental composites. J Mech Behav Biomed Mater. 2013;18:123–31.

24. Gao L, Liu Q, Hong JS, Miyamoto H, De La Torre SD, Kakitsuji A, et al. Phase transformation in the Al2O3-ZrO2 system. J Mater Sci. 1998;33(6):1399–403.

25. Wakai F, Iga T, Nagano T. Effect of dispersion of ZrO2 particles on creep of fine-grained Al2O3. J Ceram Soc Jpn. 1988;12:1206–1209.

26. Yoshida H, Okada K, Ikuhara Y, Sakuma T. Improvement of high-temperature creep resistance in fine-grained Al2O3 by Zr4+ segregation in grain boundaries. Philos Mag Lett. 1997;76(1):9–14.

27. Kim M, Laine RM. Liquid-feed flame spray pyrolysis (LF-FSP) for combinatorial processing of nanooxide powders along the (ZrO2)1-x(Al2O3)x tie-line. Phase segregation and the formation of core-shell nanoparticles. J Ceram Process Res. 2007;8(2):129–36.

28. Kim M, Laine RM. Pressureless sintering t-zirconia@δ-Al2O3 (54 mol%) core-shell nanopowders at 1120°C provides dense t-zirconia-toughened α-Al2O3 nanocomposites. J Am Ceram Soc. 2010;93(3):709–15.

29. Kim M. Mixed-metal oxide nanopowders by liquid-feed flame spray pyrolysis (LF-FSP): synthesis and processing of core-shell nanoparticles [Thesis]. Ann Arbor (MI): University of Michigan; 2008.

30. Zhao Z, Zhang L, Song Y, Wang W, Wu J. Microstructures and properties of rapidly solidified Y2O3 doped Al2O3/ZrO2 composites prepared by combustion synthesis. Scr Mater. 2006;55(9):819–22.

31. Pena JI, Merino RI, Harlan NR, Larrea A, De la Fuente GF, Orera VM. Microstructure of Y2O3 doped Al2O3-ZrO2 eutectics grown by the laser floating zone method. J Eur Ceram Soc. 2002;22(14–15):2595–602.

32. Lee JH, Yoshikawa A, Kaiden H, Lebbou K, Fukuda T, Yoon DH, et al. Microstructure of Y2O3 doped Al2O3/ZrO2 eutectic fibers grown by the micro-pulling-down method. J Cryst Growth. 2001;231(1–2):179–85.

33. Yoshida H, Kuwabara A, Yamamoto T, Ikuhara Y, Sakuma T. High temperature plastic flow and grain boundary chemistry in oxide ceramics. J Mater Sci. 2005;40(12):3129–35.

34. Yi E, Wang W, Mohanty S, Kieffer J, Tamaki R, Laine RM. Materials that can replace liquid electrolytes in Li batteries: Superionic conductivities in Li1.7Al0.3Ti1.7Si0.4P2.6O12. Processing combustion synthesized nanopowders to free standing thin films. J Power Sources. 2014;269(10):577–588.

35. Yi E, Wang W, Kieffer J, Laine RM. Flame made nanoparticles permit processing of dense, flexible, Li+ conducting ceramic electrolyte thin films of cubic-Li7La3Zr2O12 (c-LLZO). J Mater Chem A. 2016;4(33):12947–54.

36. Yi E, Temeche E, Laine RM. Superionically conducting β″-Al2O3 thin films processed using flame synthesized nanopowders. J Mater Chem A. 2018;6:12411–9.

37. Wang CJ, Huang CY. Effect of TiO2 addition on the sintering behavior, hardness and fracture toughness of an ultrafine alumina. Mater Sci Eng A. 2008;492(1–2):306–10.

38. Bagley RD, Cutler IB, Johnson DL. Effect of TiO2 on initial sintering of Al2O3. J Am Ceram Soc. 1970;53(3):136–141.

39. Brook RJ. Effect of TiO2 on initial sintering of Al2O3. J Am Ceram Soc. 1972;55(2):114–114.

40. Roy SK, Coble RL. Solubilities of magnesia, titania, and magnesium titanate in aluminum oxide. J Am Ceram Soc. 1968;51(1):1–6.

41. Kosmac T, Wallace JS, Claussen N. Influence of MgO additions on the microstructure and mechanical properties of Al2O3-ZrO2 composites. J Am Ceram Soc. 1982;65(5):c66–67.

42. Coble RL. Sintering crystalline solids. II. experimental test of diffusion models in powder compacts. J Appl Phys. 1961;32(5):793–9.

43. Bennison SJ, Harmer MP. Grain-growth kinetics for alumina in the absence of a liquid phase. J Am Ceram Soc. 1985;68(1):C–22–C–24.

44. Berry KA, Harmer MP. Effect of MgO solute on microstructure development in Al2O3. J Am Ceram Soc. 1986;69(2):143–149.

45. Shaw NJ, Brook RJ. Structure and grain coarsening during the sintering of alumina. J Am Ceram Soc. 1986;69(2):107–110.

46. Greskovich C, Brewer JA. Solubility of magnesia in polycrystalline alumina at high temperatures. J Am Ceram Soc. 2001;84(2):420–425.

47. Bennison SJ, Harmer MP. Effect of magnesia solute on surface diffusion in sapphire and the role of magnesia in the sintering of alumina. J Am Ceram Soc. 1990;73(4):833–837.

48. Rhamdhani MA, Soepriyanto S, Ramelan A, Barliansyah A. Determination of mechanism and grain growth kinetics of MgO doped Al2O3. J Trop Med. 2005;12(3):148–158.

49. Lin FJT, De Jonghe LC. Initial coarsening and microstructural evolution of fast-fired and MgO-doped Al2O3. J Am Ceram Soc. 1997;80(11):2891–2896.

50. Kottada RS, Chokshi AH. The high temperature tensile and compressive deformation characteristics of magnesia doped alumina. Acta Mater. 2000;48(15):3905–15.

51. Yoshizawa Y, Sakuma T. Improvement of tensile ductility in high-purity alumina due to magnesia addition. Scanning. 1992;40(11):2943–2950.

52. Backhaus-Ricoult M, Guerin V, Huntz A-M, Urbanovich VS. High-temperature oxidation behavior of high-purity α-, β-, and mixed silicon nitride ceramics. J Am Ceram Soc. 2002;85(2):385–392.

53. Raider SI, Flitsch R, Aboaf JA, Pliskin WA. Surface oxidation of silicon nitride films. J Electrochem Soc. 1976;123(4):560–565.

54. Narushima T, Goto T, Hirai T, Iguchi Y. High-temperature oxidation of silicon carbide and silicon nitride. Mater Trans JIM. 1997;38(10):821–35.

55. Andrews P, Riley FL. The microstructure and composition of oxide films formed during high temperature oxidation of a sintered silicon nitride. J Eur Ceram Soc. 1989;5(4):245–56.

56. Zhou Y, Hyuga H, Kusano D, Yoshizawa Y, Hirao K. A tough silicon nitride ceramic with high thermal conductivity. Adv Mater. 2011;23(39):4563–7.

57. Fukuda S, Shimada K, Izu N, Miyazaki H, Iwakiri S, Hirao K. Crack generation in electroless nickel plating layers on copper-metallized silicon nitride substrates during thermal cycling. J Mater Sci Mater Electron. 2017 (Jun);28(11):8278–85.

58. Hirao K, Fukuda S, Miyazaki H, Zhou Y, Hyuga H, Iwakiri S. Evaluation of residual thermal stress in Cu metalized silicon nitride substrates by raman spectroscopy. In: 2018 International Conference on Electronics Packaging and iMAPS All Asia Conference (ICEP-IAAC) [Internet]. 2018. p. 194–6. Available from: https://doi.org/10.23919/ICEP.2018.8374701.

59. Kim S, Gislason JJ, Morton RW, Pan XQ, Sun HP, Laine RM. Liquid-feed flame spray pyrolysis of nanopowders in the alumina-titania system. Chem Mater. 2004;16(12):2336–43.

60. Kim M, Laine RM. One-step synthesis of core-shell (Ce0.7Zr0.3O 2)x(Al2O3)1-x [(Ce 0.7Zr0.3O2)@Al2O3] nanopowders via liquid-feed flame spray pyrolysis (LF-FSP). J Am Chem Soc. 2009;131(26):9220–9.

61. Kim M, Hinklin TR, Laine RM. Core-shell nanostructured nanopowders along (CeOx) x(Al2O3)1-x tie-line by liquid-feed flame spray pyrolysis (LF-FSP). Chem Mater. 2008;20(16):5154–62.

62. Laine RM, Marchal J, Sun H, Pan XQ. A new Y3Al5O12 phase produced by liquid-feed flame spray pyrolysis (LF-FSP). Adv Mater. 2005;17(7):830–3.

63. Wei GC, Rhodes WH. Sintering of translucent alumina in a nitrogen–hydrogen gas atmosphere. J Am Ceram Soc. 2000;83(7):1641–8.

Tables

Table 1. Comparison of ZTA ceramics in literature and this work.

ZrO_2 (%)[a]	t (%)[b]	Powder processing/synthesis	Sintering condition (°C/h)	AGS (μm)[c]	Relative density (%)	Mechanical properties[d]	Ref.
5-20 vol.	10-90	Ball milling	1500/2, hot-pressing	0.4-5	-	K_{1C}: 6-8 H_v: 10-12	20
5-30 vol. (3Y)	50-100	Ball milling	1600/1/air	0.3-3	96-99	E: 340-390 σ: 400-950	21
5 mol.	75	Sol-gel	1550/4/air	0.1-4	98	E: 370 K_{1C}: 5	4,5

						H_v: 17	
30 wt. (3Y)	100	GCHAS[e]	1600/1/air	0.6-4	92	K_{1C}: 5.5 H_v: 14-15 σ: 610	6
20 wt. (10M)	25	Ball milling	1600/2/air	~1	94.5	K_{1C}: 11.5 H_v: 16.4	23
10-30 wt. (3Y)	8-25	Co-precipitation	1600/5/air	0.5-3	96-98	K_{1C}: 8-8.5	2
54 mol.	100	LF-FSP	1120/6/air	~0.2	99	-	27–29
10 mol.[f]	100	LF-FSP	1500/5/N_2/H_2	0.5-1	97-99	K_{1C}: 24	This work

[a]ZrO_2 content, *t*-ZrO_2 stabilizing additives: 3Y = 3 mol. % Y_2O_3, 10M = 10 wt. % MgO. [b]*t*-ZrO_2 content in sintered ceramics at room temperature. [c]Average grain sizes of both Al_2O_3 and ZrO_2. [d]K_{1C}: fracture toughness (MPa $m^{1/2}$); H_v: Vickers hardness (GPa); E: elastic modulus (GPa); σ: flexural strength (MPa). [e]Gel casting hydrolysis-assisted solidification. [f]One example is given: 10 mol. % ZrO_2 doped Al_2O_3 films (~200 μm thick) with MgO and TiO_2 (1 wt. % each).

Table 2. Selected properties of $(ZrO_2)_x(Al_2O_3)_{1-x}$ (x = 0, 15, 30, 50 mol. %) nanopowders.

ZrO_2 content, mol. %	ZrO_2 content, wt. %	Density*, g/cm^3	SSA, m^2/g	APS, nm
0	0	3.95	49 ± 0.5	31 ± 0.3
15	17.6	4.25	50 ± 0.5	28 ± 0.3
30	34.1	4.54	53 ± 0.5	25 ± 0.2
50	54.7	4.90	40 ± 0.3	30 ± 0.3

Table 3. Compositions of ZTA films.

Composition	ZrO_2 content	Dopants, wt. %
A	30 mol. %	-
B	30 mol. %	1 wt. % TiO_2 CP[a]
C	30 mol. %	1 wt. % TiO_2 NP[b]
D[c]	10 mol. %	1 wt. % TiO_2 NP, 1 wt. % MgO

[a]CP: commercial powder from Evonik Industries AG, Germany. APS ≈ 20 nm but may be agglomerated. [b]NP: nanopowder by LF-FSP, APS = 20-30 nm. [c]A mixture of LF-FSP produced 30 mol. % ZrO_2 doped Al_2O_3, 2 wt. % MgO doped Al_2O_3,[10] and 1 wt. % TiO_2 NP.

Table 4. Lateral shrinkage of ZTA films (**A**-**D** per Table **3**) sintered at 1400-1500 °C/5 h/N_2/H_2.

Sintering condition	Lateral shrinkage, %			
	A	B	C	D
1400 °C/5 h/N_2/H_2	14	10	14	12
1450 °C/5 h/N_2/H_2	16	19	22	18
1500 °C/5 h/N_2/H_2	24	25	24	22
1500 °C/5 h/O_2	19	25	22	22

Table 5. AGSs and shrinkages of ZTA films (composition **D**, size ≈ 1×1 cm^2 × 200 μm).

Sintering condition	AGS, μm	Lateral shrinkage, %	Vertical shrinkage, %
1500 °C/5 h/O_2	0.9 ± 0.2	19	17
1500 °C/5 h/N_2/H_2	0.8 ± 0.2	22	24

Table 6. Selected properties of ~200 μm ZTA films (composition **D**) sintered at 1500 °C/5 h/N_2/H_2 with different sintering ramp rates.

Ramp rate, °C/min	AGS, μm	Lateral shrinkage, %	Vertical shrinkage, %	Measured density*, g/cm^3	Theoretical density*, g/cm^3	Relative density, %
5	1.3 ± 0.3	20	16	3.62	4.04	89.7
2.5	1.5 ± 0.3	22	24	3.66	4.03	90.7
1	1.6 ± 0.4	23	23	3.68	4.04	91.2

*Film densities are measured by the Archimedes method; theoretical densities are calculated from phase compositions analyzed by XRD refinement.

Table 7. Selected properties of ~200 μm ZTA films (composition **D**) sintered at different binder burnout conditions with BN insulation.

Binder burnout condition	AGS, μm	Lateral shrinkage, %	Vertical shrinkage, %	Measured density, g/cm^3	Theoretical density, g/cm^3	Relative density, %
600 °C/1h/air	0.7 ± 0.1	20	20	4.05	4.10	98.8
800 °C/1h/air	0.8 ± 0.1	21	21	4.07	4.12	98.8
1100 °C/1h/air	1.1 ± 0.1	N/A*	21	4.00	4.12	97.1

3-step burnout	0.7 ± 0.1	17	19	4.02	4.10	98.1

*Films debindered at 1100 °C/1h/air cracked into pieces and failed to give accurate lateral lengths after sintering.

Figure captions

Scheme 1. Liquid feed flame spray pyrolysis (LF-FSP) for nanopowder production.

Figure 1. XRDs of $(ZrO_2)_x(Al_2O_3)_{1-x}$ (x = 0, 15, 30, 50 mol. %) NPs.

Figure 2. SEM fracture surfaces of sintered $(ZrO_2)_x(Al_2O_3)_{1-x}$ (x = 0, 15, 30, 50 mol. %) thin films.

Figure 3a. AGSs vs ZrO_2 content **b.** sintered film thicknesses for $(ZrO_2)_x(Al_2O_3)_{1-x}$ (x = 0, 15, 30, 50 mol. %).

Figure 4. SEM fracture surfaces of ZTA films (**A**-**D** per Table **3**) sintered at 1300-1500 °C/5 h/O_2. The red arrow suggests transgranular fracture.

Figure 5. XRDs of ZTA films (**A**-**D** per Table **3**) sintered at 1300-1500 °C/5 h/O_2.

Figure 6. SEM fracture surfaces of ZTA films (**A**-**D** per Table **3**) sintered at 1400-1500 °C/5 h/N_2/H_2. Red arrows suggest transgranular fracture.

Figure 7. SEM fracture surfaces of ZTA films (composition **D**, size ≈ 1×1 cm^2 × 200 μm) sintered at 1500 °C/5 h/O_2 (a, c) and 1500 °C/5 h/ N_2/H_2 (b, d). Initial thickness ≈ 200 μm before sintering.

Figure 8. SEM fracture surfaces of ~200 μm ZTA films (composition **D**) sintered (1500 °C/5 h/N_2/H_2) at 5 °C/min (a, d), 2.5 °C/min (b, e) and 1 °C/min (c, f). Green film thicknesses were 220-250 μm before sintering.

Figure 9. Optical images of ~200 μm ZTA films (composition **D**) before and after binder burnout and sintering (see schedule in Figure **S14**). Thicknesses are given on the films, and lateral lengths are given on the right.

Figure 10. SEM fracture surfaces of ~200 μm ZTA film (composition **D**) sintered with 3-step binder burnout procedure per Figure **S14**.

Figure 11. Representative examples (a) and dye test (b) of Si_3N_4 films coated with ZTA (composition **D**) after sintering at 1500 °C/5 h/N_2/H_2.

Figure 12. SEM fracture surface (a) and surface (b) of Si_3N_4 films coated with ZTA (composition **D**) sintered at 1500 °C/5 h/N_2/H_2. **c**. SEM surface of an uncoated Si_3N_4 film.

Figure 13. XRDs of Si_3N_4 films coated with ZTA (composition **D**) sintered at 1500 °C/5 h/N_2/H_2.

Figure 14. Optical images of **a**. uncoated and **b**. coated Si_3N_4 films and SEM surfaces of **c**. uncoated and **d**. coated Si_3N_4 films with ZTA (composition **D**) after heating at 1500 °C/1 h/O_2.

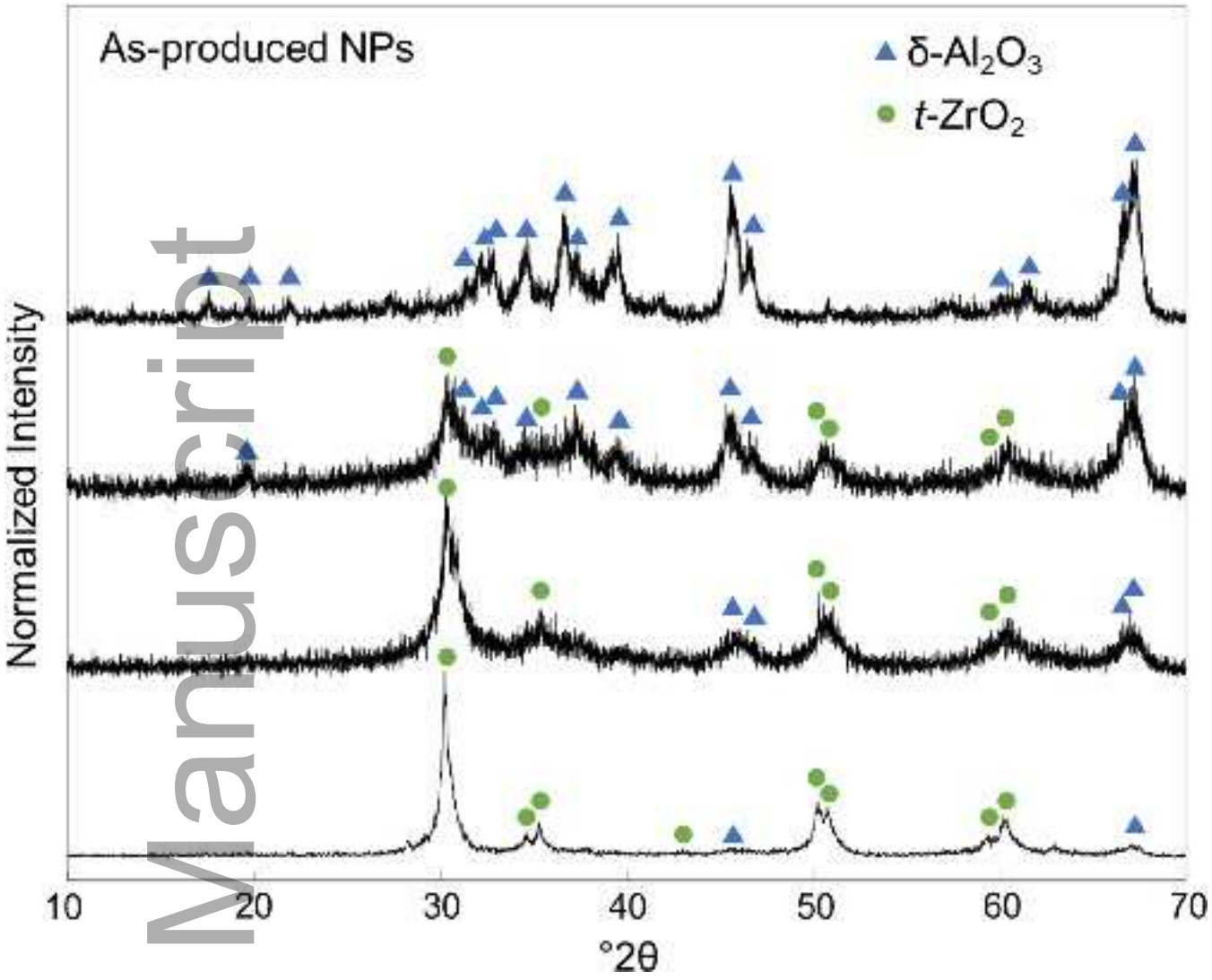

jace_17570_f1.tif

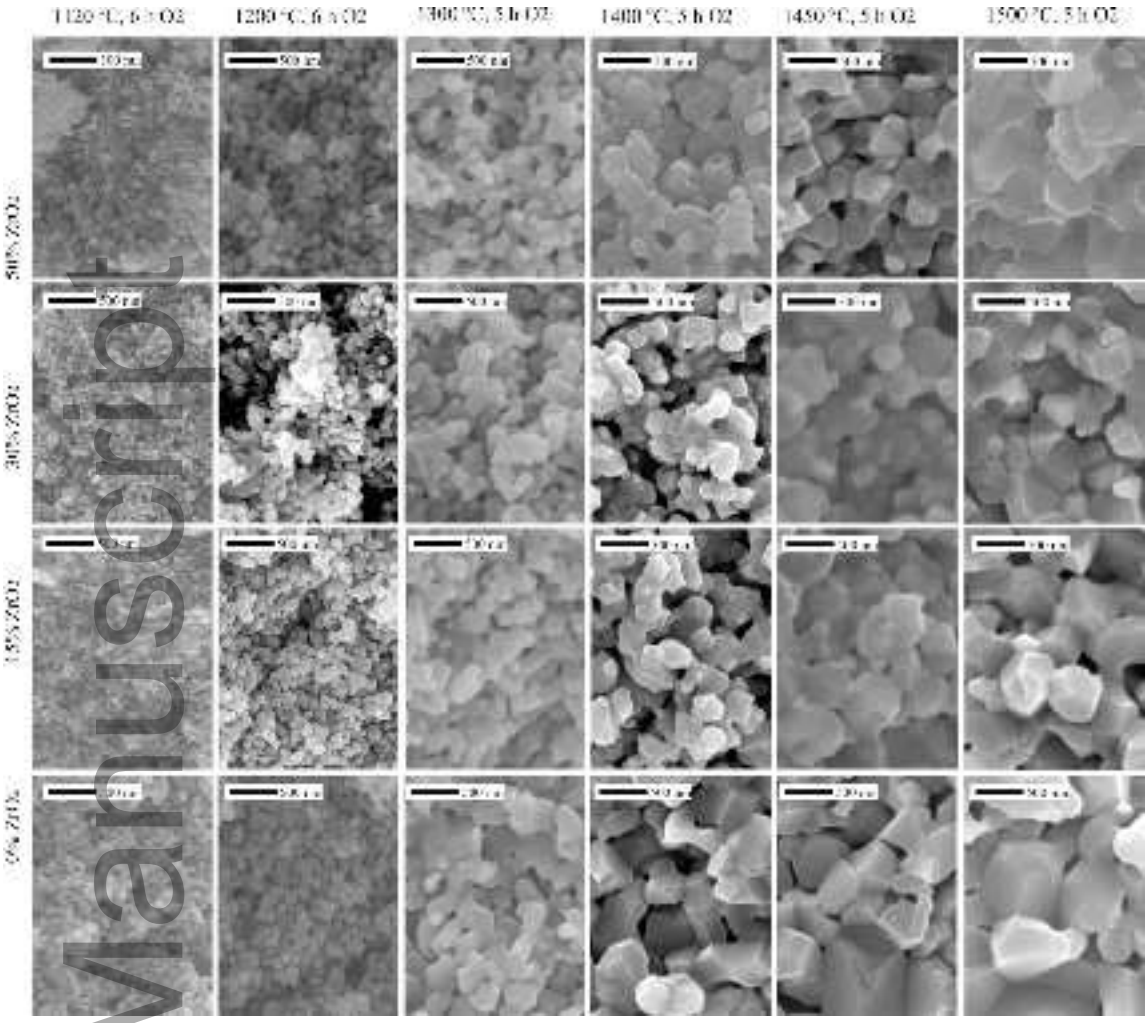

jace_17570_f2.tif

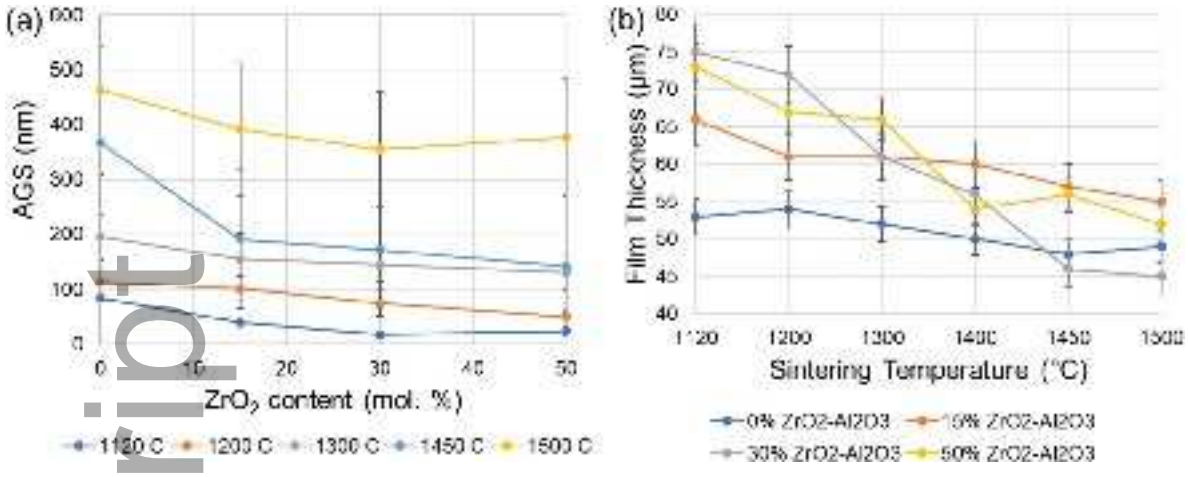

jace_17570_f3.tif

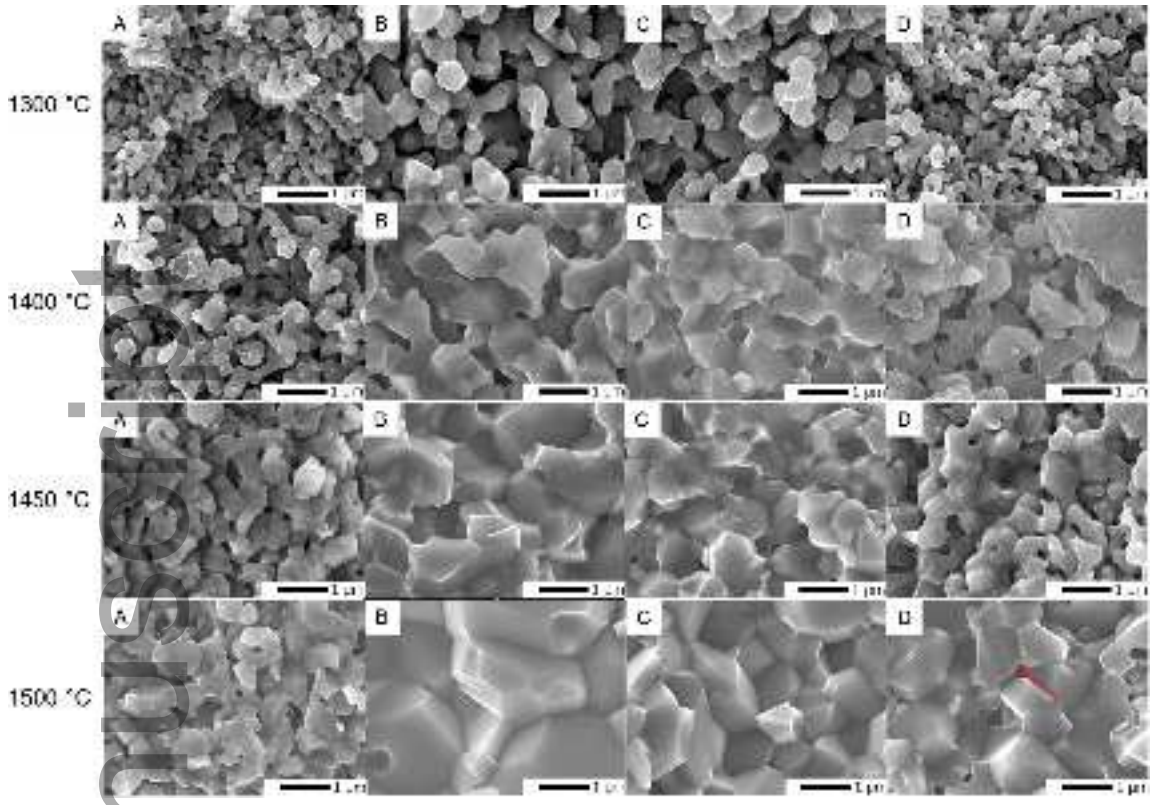

jace_17570_f4.tif

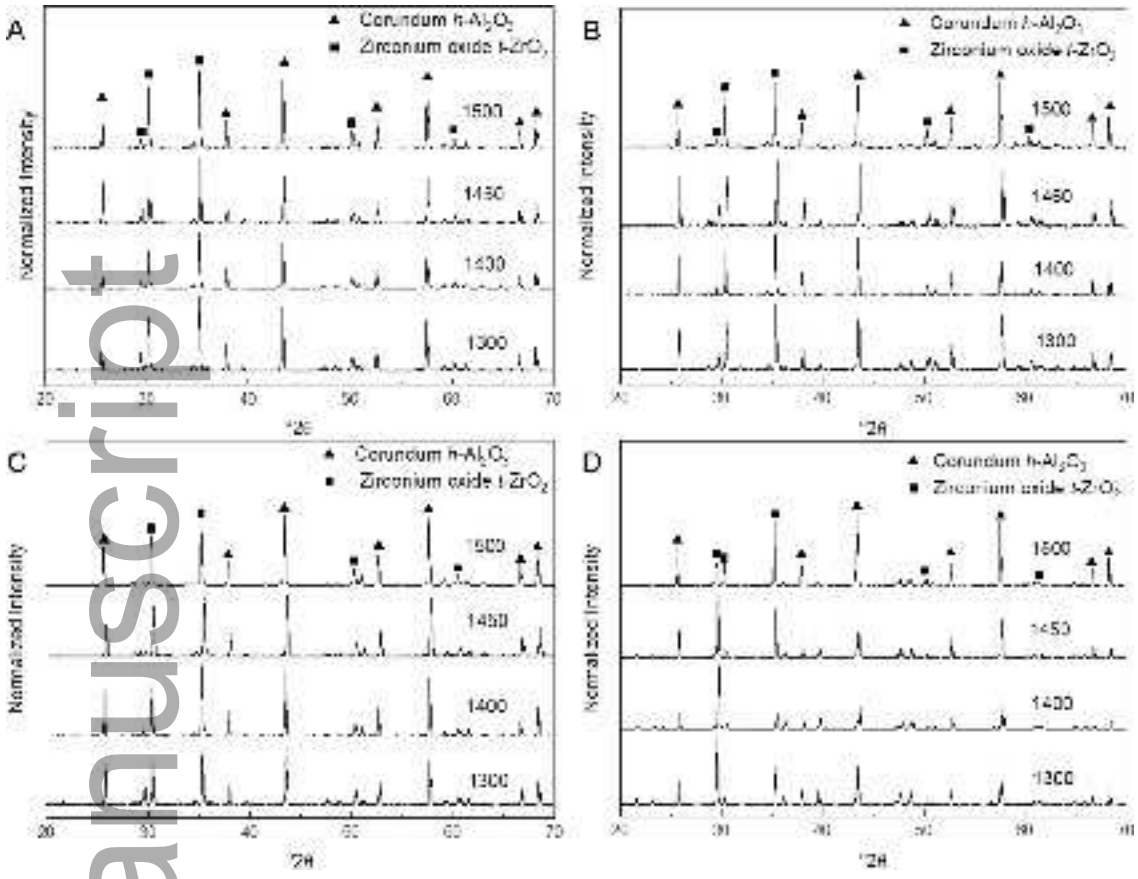

jace_17570_f5.tif

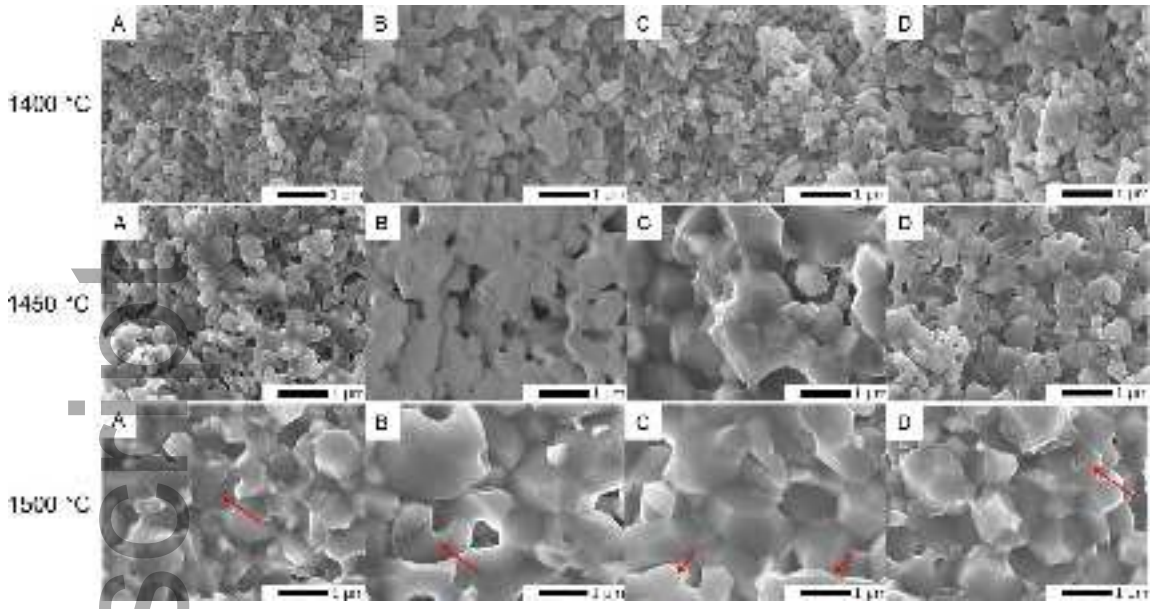

jace_17570_f6.tif

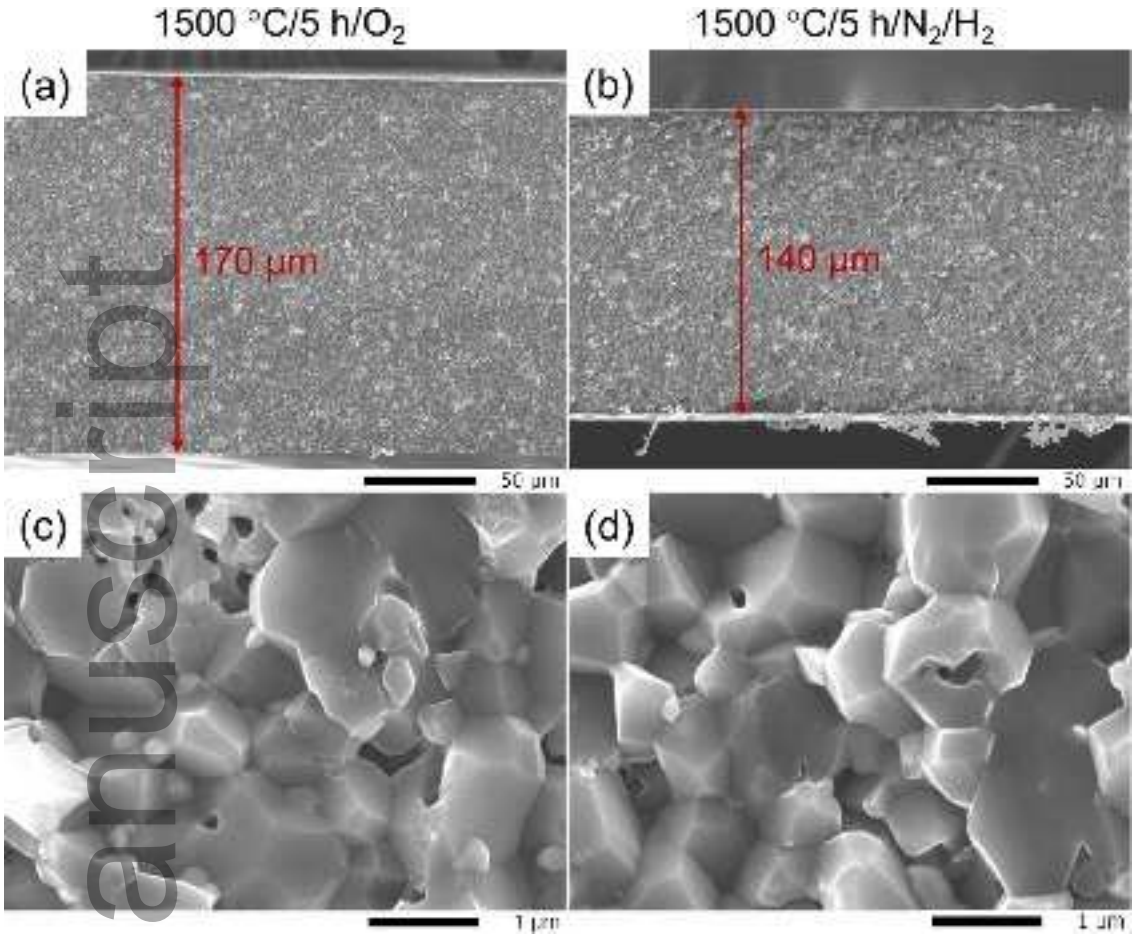

jace_17570_f7.tif

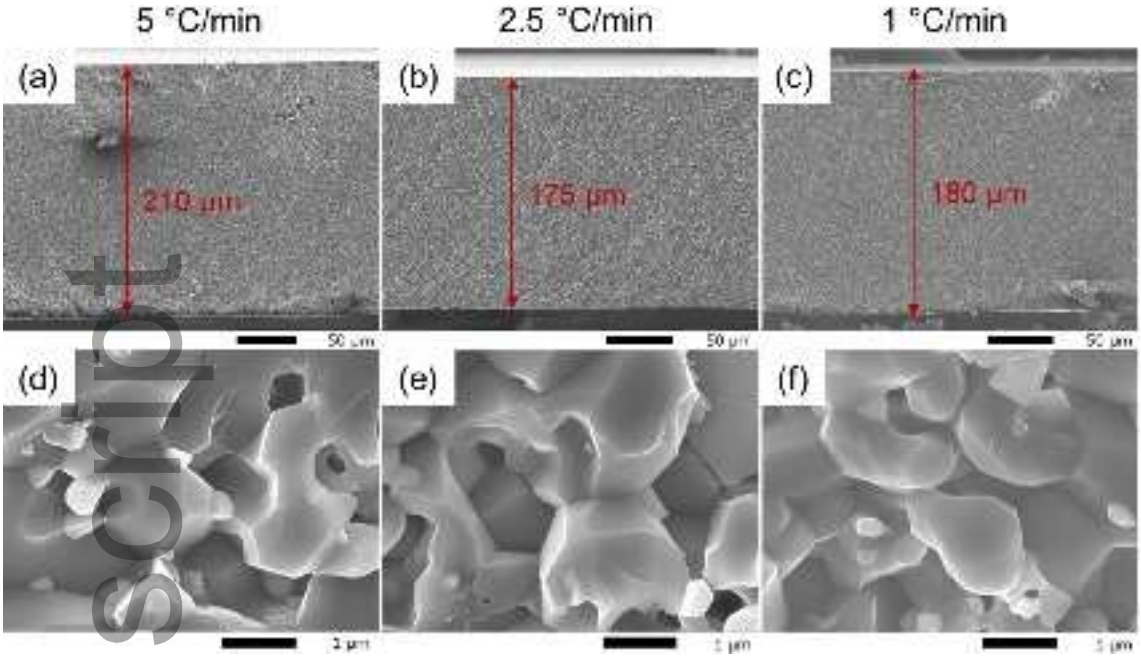

jace_17570_f8.tif

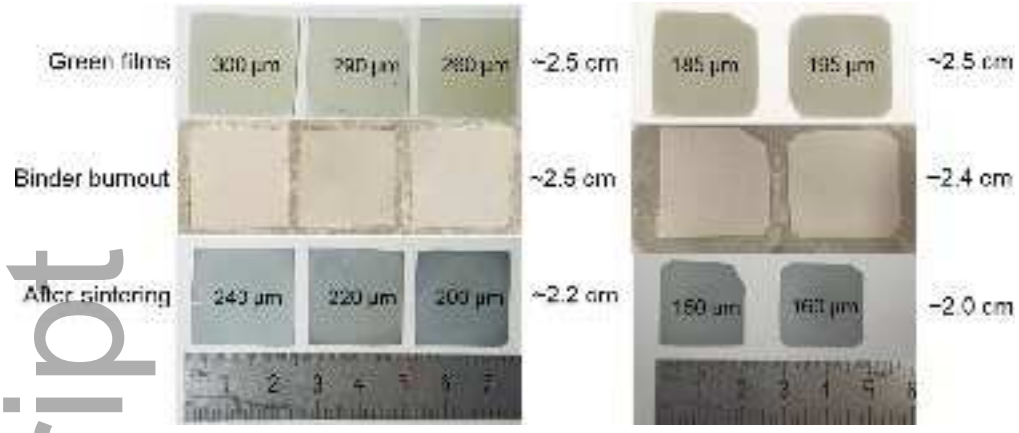

jace_17570_f9.tif

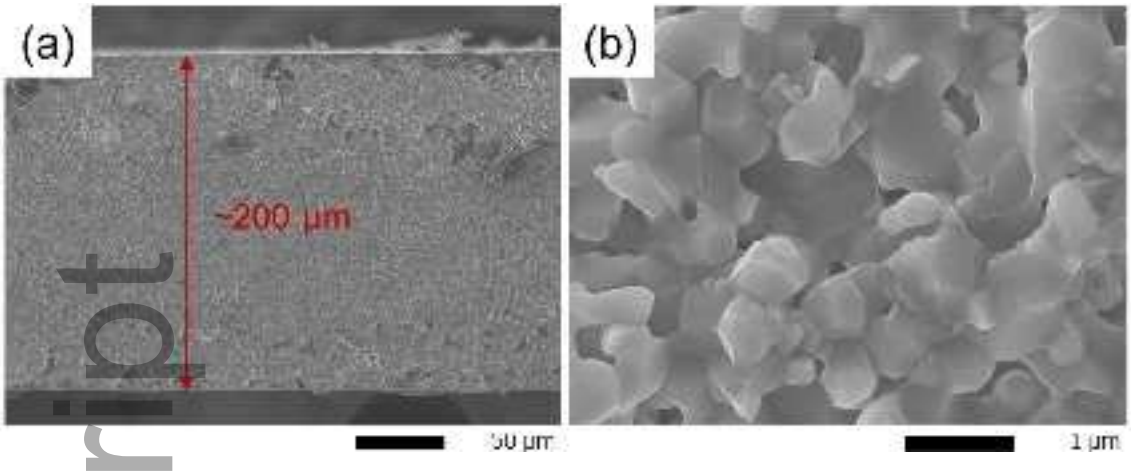

jace_17570_f10.tif

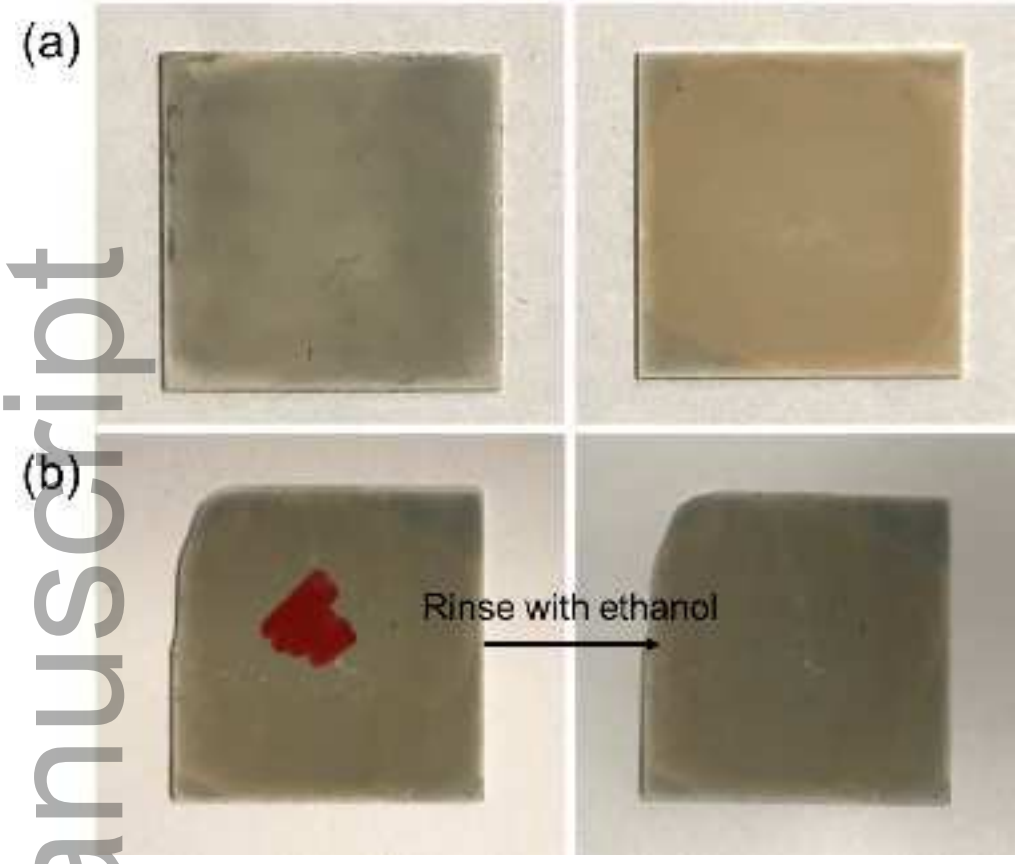

jace_17570_f11.tif

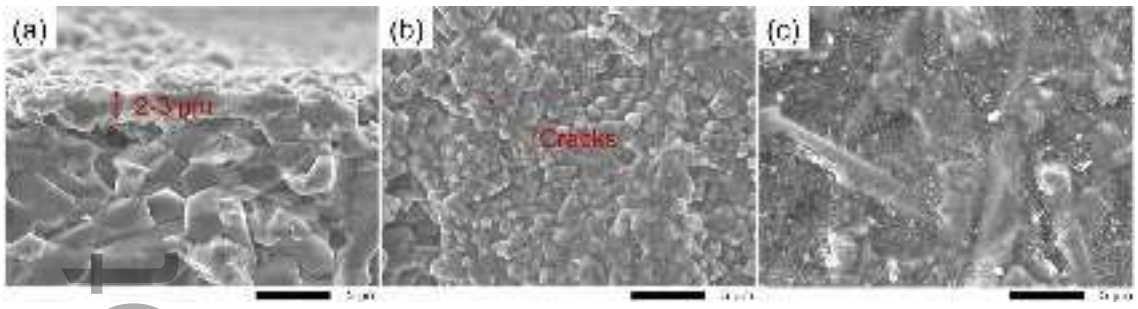

jace_17570_f12.tif

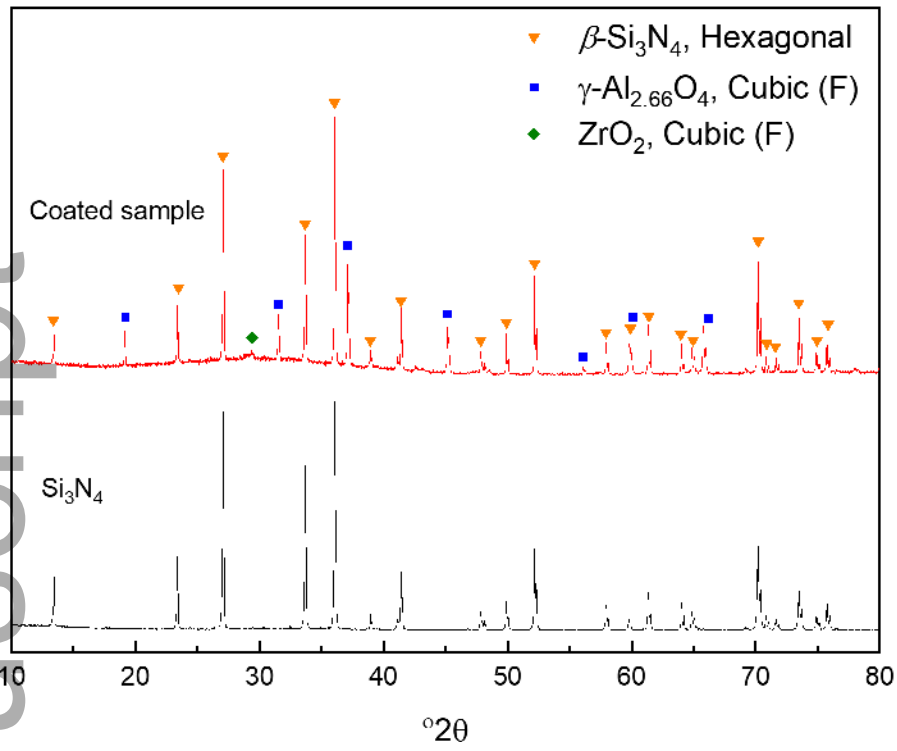

jace_17570_f13.tif

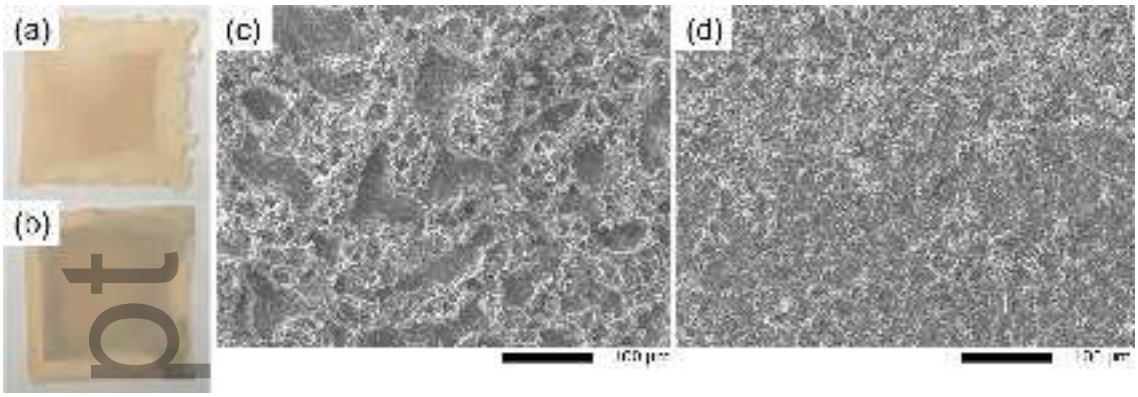

jace_17570_f14.tif